RSC Advances

REVIEW

View Article Online
View Journal | View Issue

Cite this: *RSC Adv.*, 2025, **15**, 36656

Resistance model approach for gas separation in mixed-matrix membranes: progress and applications

Juan Zhao, HongRu Ai,* Ju Guan and RenDao Wang

Received 4th August 2025
Accepted 15th September 2025

DOI: 10.1039/d5ra05684e

rsc.li/rsc-advances

Mixed-matrix membranes (MMMs) exhibit both high permeability and selectivity, with the potential to surpass the Robeson upper bound, and are therefore a major focus of research on gas separation membranes. In this review, the basic assumptions and limitations of the widely used resistance model approach (RMA) for predicting the permeability of MMMs are discussed. Additionally, the practical application of the RMA in optimizing membrane structure design is introduced. By comparing prediction results with experimental data, the applicability of these models in predicting the permeability of MMMs is revealed. Finally, future development directions for the model are proposed. This review aims to provide a theoretical foundation and guidance for the design and optimization of high-performance gas separation membrane materials.

1. Introduction

Many techniques, including adsorption, absorption, cryogenic distillation and membranes, have been used for gas separation processes.[1] Among these methods, membrane technology has received significant attention for its environmental friendliness, high performance, operational simplicity, and energy efficiency.[2] It has been widely applied in air separation, oxygen/nitrogen enrichment, and olefin/paraffin separation, among other fields.[1,2] The permeability and selectivity of gas separation membranes are two critical performance metrics. The selectivity of gas separation membranes represents the degree of separation of the required gas molecules from other molecules, and the separation factor represents the efficiency of gas separation.[3]

Mixed-matrix membranes (MMMs), which consist of two phases, a polymer matrix and a dispersed phase, have attracted considerable attention in recent years due to their exceptional separation and permeability performance.[4–6] With the rapid development of inorganic fillers, inorganic materials with high specific surface areas, tunable structures, and superior porous properties have been increasingly explored.[7–10] Three-dimensional (3D) inorganic materials (*e.g.*, bulk MOFs and mesoporous silica frameworks) exhibit inherent advantages of well-developed porous networks and high loading capacity, and they are often used as functional additives to optimize the pore structure of MMMs or as templates for fabricating 1D/2D derivatives. However, their relatively large spatial size may lead to challenges in uniform dispersion within membrane matrices, limiting their widespread application. It has been found that the performance enhancement of MMMs can be maximized when high-aspect-ratio fillers such as zeolite and MOF nanosheets are used instead of isotropic particles (*e.g.*, 3D MOFs).[11] High-aspect-ratio fillers are known for offering tortuous pathways, particularly for nonpermeable molecules. At the same time, permeable gas can easily permeate through the composite membranes, which can significantly enhance gas selectivity based on diffusion pathway difference.[12,13]

Accordingly, two-dimensional materials with atomic-level thickness and precise molecular sieving capabilities (*e.g.*, graphene and MOF nanosheets) and one-dimensional materials with smooth inner walls that provide linear mass transfer pathways (*e.g.*, carbon nanotubes) have been widely utilized in gas separation membranes, achieving remarkable permeability and selectivity.[14–16]

However, the development of permeability models for MMMs lags behind experimental progress, and membrane material screening still relies heavily on extensive trial-and-error experiments, which hinder the advancement and application of these materials. Therefore, there is an urgent need to establish an accurate model for predicting the permeability and selectivity of gas separation membranes to accelerate material screening.

Currently, macroscopic approaches for predicting the permeability of MMMs primarily include the resistance model approach (RMA), effective medium approach (EMA), and simulation-based rigorous modeling approach (SMA).[17–22] Meso- and micro-scale analytical methods encompass molecular simulation, molecular simulation-Maxwell methods, and density functional theory.[23–27]

By analogizing gas permeation resistance to series-parallel resistor networks, RMA explicitly accounts for critical factors

School of Chemical Engineering, Guizhou University of Engineering Science, Bijie 551700, P. R. China. E-mail: zhaojhld123@sina.com

such as filler orientation, distribution, aspect ratio, and interfacial characteristics, which are key parameters governing the performance of MMMs incorporating tubular or flake-like nanostructures. Given this inherent advantage, the present study specifically selects RMA as the core framework to systematically evaluate theoretical principles, application boundaries, and the practical value of the approach in membrane optimization.

Despite extensive literature on modelling techniques,[14,17,18,28–34] few studies effectively bridge the gap between theoretical models and practical applications. Particularly in membrane structure design and optimization, systematic model-driven methodologies remain exceptionally scarce, which significantly limits the practical utility of computational models and hinders their potential in guiding membrane material fabrication processes.

To address this scarcity and bridge the critical gap between theoretical prediction and practical design, the present study proposes an integrative analytical framework based on the Resistance Model Approach (RMA). This framework deciphers the intricate morphology/structure–performance correlations in MMMs, moving beyond simple permeability prediction. By systematically categorizing and evaluating classical RMA-based models, we elucidate their underlying physical principles and, more importantly, their applicability boundaries, which are governed by filler geometry (cubic, flake-like, and tubular) and interface morphology (ideal, rigidified, and leaky). Furthermore, this work demonstrates the practical utility of this framework for optimizing membrane structure by quantitatively delineating mass-transfer pathways, characterizing filler effects, and elucidating interface mechanisms. We aim to provide a systematic, model-driven methodology that translates theoretical insights into actionable guidance for the rational design of high-performance MMMs, ultimately moving beyond the current trial-and-error paradigm. Finally, the future developmental trends of the models are explored in detail. This review thus provides a valuable reference and guidance for subsequent endeavors in the preparation of novel gas separation membranes.

2. Resistance model approach (RMA)

The basic assumption of the resistance model is that flake-like, cubic, or tubular fillers are oriented and uniformly distributed in the polymer matrix. The resistance model approach (RMA) relies on the analogy between the current flow through a series-parallel array of resistors (Ohm's law) and the permeation rate through an MMM (Fick's law).[35–37] Under this consideration, the MMM permeability is inversely proportional to the overall transport resistance. Then, through theoretical derivation, the relationship between the effective permeability coefficient of the MMM and the corresponding equivalent resistance is obtained,[38–40] as shown in eqn (1).

$$R_{\mathrm{eff}} = l/(P_{\mathrm{eff}} \cdot A) \quad (1)$$

Here, R_{eff} and P_{eff} are the overall transport (permeation) resistance and the MMM permeability, respectively, l is the membrane thickness, and A is the cross-sectional area in the flow direction.

It is noteworthy that the RMA is particularly advantageous for modelling MMMs containing anisotropic fillers (*e.g.*, flakes and tubes), where the transport path is highly directional. For MMMs incorporating conventional isotropic 3D fillers (*e.g.*, spherical zeolites and MOFs), effective medium theory (EMT) models, such as the Maxwell model, are more prevalent due to their simplicity and effectiveness in describing systems with randomly dispersed spherical inclusions.[17,28] This review focuses on RMA due to its unique strength in addressing the increasingly important class of anisotropic nanofillers.

2.1 Series and parallel resistance models

The simplest resistance model is the two-resistance (polymer R_{m} and filler R_{f}) model proposed by Zimmerman *et al.*,[41] which includes series and parallel models. Following the electrical circuit analog and the above definition for the permeation resistance in eqn (1), the permeability for the multilayer composite in series yields eqn (2), as shown in Table 1, while that of a multilayer composite in parallel yields eqn (3). The two-resistance model introduces the permeability of the polymer matrix (P_{m}), the permeability of the filler (P_{f}), and the volume fraction of the filler (φ_{f}) as model parameters. Although the two-resistance model is very simple, it provides important reference boundaries for the permeation performance of ideal MMMs. The series model in eqn (2) is assumed to provide the lower bound for the permeability of a given penetrant in an ideal MMM. Alternatively, the parallel model in eqn (3) is assumed to provide the upper bound for the effective permeability of a given penetrant in an ideal MMM.

While the series and parallel models provide a simplistic framework, their true value lies in establishing the fundamental theoretical bounds for MMM performance. This delineation of upper and lower limits reveals the critical insight that the actual spatial distribution and morphology of the filler constitute the paramount factor governing membrane properties. The vast performance gap between these bounds depends primarily on whether the filler's morphology forces gases to navigate around it, which increases tortuosity and approaches the series limit, or creates direct pathways for gases to flow through it, moving closer to the parallel scenario. This central role of morphology in determining transport pathways motivates the development of more sophisticated resistance models, such as the Te Hennepe model, discussed next, which aim to quantitatively capture these complex structural effects.

When there are large differences in permeabilities between the filler and polymer phases or defects in the MMM structure, the diffusion path of gas molecules in the MMM will exhibit a tortuous effect, resulting in deviations in concentration flow lines. Therefore, additional diffusion resistances must be considered to account for tortuosity effects in the permeant diffusion path. Recently, more complex models, including three resistances or more, have been proposed following the RMA in order to reveal the influence of the tortuosity effects on the permeability of MMMs.

Table 1 Permeability models based on the resistance model approach

Model	Permeability equations	Resistance direction	Equation number
Zimmerman-series[41]	$P_{\text{eff}} = \dfrac{P_{\text{m}}P_{\text{f}}}{P_{\text{m}}\varphi_{\text{f}} + P_{\text{f}}(1-\varphi_{\text{f}})}$		(2)
Zimmerman-parallel[41]	$P_{\text{eff}} = P_{\text{f}}\Phi_{\text{f}} + P_{\text{m}}(1-\Phi_{\text{f}})$	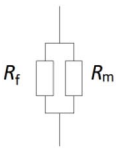	(3)
Te Hennepe[42]	$P_{\text{eff}} = P_{\text{m}}\left[\left(1-\varphi_{\text{f}}^{\frac{1}{3}}\right) + \dfrac{\frac{3}{2}\varphi_{\text{f}}^{\frac{1}{3}}P_{\text{m}}}{P_{\text{m}}(1-\varphi_{\text{f}}) + \frac{3}{2}P_{\text{f}}\varphi_{\text{f}}}\right]^{-1}$	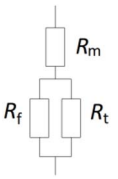	(4)
Cussler[45]	$P_{\text{eff}} = P_{\text{m}}\left[(1-\varphi_{\text{f}}) + \left(\dfrac{P_{\text{f}}}{\varphi_{\text{f}}P_{\text{m}}} + \dfrac{4(1-\varphi_{\text{f}})}{{\lambda_{\text{f}}}^2{\varphi_{\text{f}}}^2}\right)^{-1}\right]^{-1}$	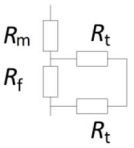	(5)
Ebneyamini[46]	$P_{\text{eff}} = \tau\left[\left(1-\varphi_{\text{f}}^{\frac{2}{3}}\right)P_{\text{m}} + \dfrac{P_{\text{m}}P_{\text{f}}\varphi_{\text{f}}^{\frac{2}{3}}}{\varphi_{\text{f}}^{\frac{1}{3}}P_{\text{m}} + \left(1-\varphi_{\text{f}}^{\frac{1}{3}}\right)P_{\text{f}}}\right]$	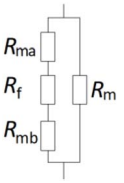	(6)
	$P_{\text{f}}/P_{\text{m}} > 1: \quad \tau(P_{\text{m}}, P_{\text{f}}, \varphi_{\text{f}}) = 1 + \dfrac{C_{\text{M}}b\left(\frac{P_{\text{f}}}{P_{\text{m}}} - 1\right)}{1 + b\left(\frac{P_{\text{f}}}{P_{\text{m}}} - 1\right)}$		(7)
	$b = -0.0923{\varphi_f}^2 - 0.0563\varphi_{\text{f}} + 0.1486$ $C_{\text{M}} = 2.2115{\varphi_{\text{f}}}^3 - 4.2545{\varphi_{\text{f}}}^2 + 2.043\varphi_{\text{f}}$		
	$P_{\text{f}}/P_{\text{m}} \leq 1: \quad \tau(P_{\text{m}}, P_{\text{f}}, \varphi_{\text{f}}) = 1 + \dfrac{C_{\text{M}}b\left(\frac{P_{\text{m}}}{P_{\text{f}}} - 1\right)}{1 + b\left(\frac{P_{\text{m}}}{P_{\text{f}}} - 1\right)}$		(8)
	$b = 1.6758{\varphi_{\text{f}}}^3 - 4.4098{\varphi_{\text{f}}}^2 + 2.734\varphi_{\text{f}}$ $C_{\text{M}} = -1.2077{\varphi_{\text{f}}}^4 + 2.7016{\varphi_{\text{f}}}^3 - 1.995{\varphi_{\text{f}}}^2 + 0.4593\varphi_{\text{f}} + 0.0418$		
KJN (ideal interface)[47]	$P_{\text{eff}}^{\text{oriented}} = P_{\text{m}}\left[\left(1 - \dfrac{\cos\theta}{(\cos\theta + \lambda_{\text{f}}\sin\theta)}\varphi_{\text{f}}\right) + \dfrac{P_{\text{m}}}{P_{\text{f}}}\left(\dfrac{1}{(\cos\theta + \lambda_{\text{f}}\sin\theta)}\right)\varphi_{\text{f}}\right]^{-1}$	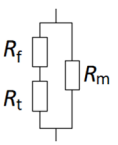	(9)
	$P_{\text{eff}}^{\text{random}} = \dfrac{\pi}{2}P_{\text{m}}\left[\int_0^{\frac{\pi}{2}} \dfrac{P_{\text{m}}}{P_{\text{eff}}^{\text{oriented}}(\theta)}\,\mathrm{d}\theta\right]^{-1}$		(10)

Table 1 (*Contd.*)

Model	Permeability equations	Resistance direction	Equation number
COF *p*-PVAm[48]	$\frac{Q_p}{Q_m} = \frac{2R_2}{R_1 + R_2} = \frac{2Q_1}{Q_1 + Q_2}$	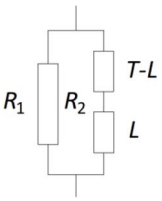	(11)
KJN (non-ideal interface)[47]	$P_{eff} = \frac{\varphi_f}{\varphi_f + \varphi_v + \varphi_p} P_{eff,f} + \frac{\varphi_v}{\varphi_f + \varphi_v + \varphi_p} P_{eff,v} + \frac{\varphi_p}{\varphi_f + \varphi_v + \varphi_p} P_P$	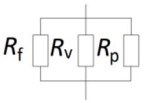	(12)
	$\frac{P_{eff,v}}{P_m} = \frac{P_v + 5P_m - 5(P_m - P_v)\varphi_v}{P_v + 5P_m + (P_m - P_v)\varphi_v}$		(13)
	$P_v = P_p = S_{IG} \cdot D_{Kn} = \frac{1}{RT} \cdot \sqrt{\frac{32r^2RT}{9\pi M}}$		(14)
mKJN[53]	$P_{eff} = \frac{\varphi_{NT}}{\varphi_{NT} + \varphi_v + \varphi_p} P_{eff,d} + \frac{\varphi_v}{\varphi_{NT} + \varphi_v + \varphi_p} P_{eff,v} + \frac{\varphi_p}{\varphi_{NT} + \varphi_v + \varphi_p} P_P$	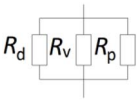	(15)
	$P_{eff,d} = \frac{P_{eff} - P_{eff,m}(1 - \varphi_d)}{\varphi_d}$		(16)
	$\frac{P_{ps}}{P_{int}} = \frac{P_{eff,v}}{P_m} = \frac{P_{NT} + 5P_{int} - 5(P_{int} - P_{NT})\varphi_s}{P_{NT} + 5P_{int} + (P_{int} - P_{NT})\varphi_s}$		(17)
	$\varphi_s = \frac{\varphi_{NT}}{\varphi_{NT} + \varphi_{int}} = \frac{{r_{NT}}^2}{(r_{NT} + l_{int})}$		(18)
	$P_{int} = S_{int} \cdot D_{int} = \frac{1}{RT} \cdot \sqrt{\frac{32{l_{int}}^2 RT}{9\pi M}}$		(19)
Hashemifard[57]	$\frac{P_{eff}}{P_m} = \left[1 + \varphi_{II}\left(\frac{1}{\varphi_{iII}({\lambda_i}^u - 1) + 1} - 1\right) + \varphi_I\left(\frac{1}{\varphi_{dI}({\lambda_d}^u - 1) + \varphi_{iI}({\lambda_i}^u - 1) + 1} - 1\right)\right]^{-u}$ $\varphi_I = \frac{\varphi}{\pi\varphi'^2}; \quad \varphi_{II} = 2^{\frac{2}{3}} 3^{\frac{1}{3}} \varphi' \theta; \quad \varphi_{III} = 1 - \varphi_I - \varphi_{II};$ $\varphi_{dI} = \pi\varphi'^2; \quad \varphi_{iI} = 4\sqrt[3]{\left(\frac{3}{2}\right)^2}\pi\varphi'^2\left(\theta^2 + \sqrt[3]{\frac{2}{3}}\theta\right); \quad \varphi_{mI} = 1 - \varphi_{dI} - \varphi_{iI};$ $\varphi_{iII} = \sqrt[3]{\left(\frac{3}{2}\right)^2}\pi\varphi'^2\left(\sqrt[3]{\left(\frac{2}{3}\right)^2} + 4\theta^2 + 4\sqrt[3]{\frac{2}{3}}\theta\right); \quad \varphi_{mII} = 1 - \varphi_{iII}$ In : $\varphi' = \sqrt[3]{\frac{\varphi}{\pi}}; \quad \theta = \frac{t}{d_p}$	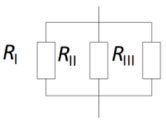 or 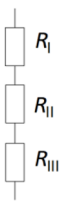	(20)

Note: P is the permeability coefficient; the subscript f denotes filler, m denotes polymer matrix, and i denotes polymer/filler interface; R_{ma} refers to the polymer permeation resistance above the filler, and R_{mb} refers to the polymer permeation resistance below the filler.

2.2 Te Hennepe model

A representative three-resistance model is the Te Hennepe model,[42] as shown in eqn (4) in Table 1. This model incorporates the tortuosity effect caused by filler shape by introducing a tortuosity factor, which is 1.5 for cubic fillers and π/2 for spherical fillers. These values represent how the presence of fillers elongates the diffusion pathways through the rubber matrix around the fillers and thus affects the transport

resistance. Originally, Te Hennepe *et al.*[42] considered the one-dimensional transport in zeolite-rubber MMMs and proposed this tortuosity factor to accurately capture the geometric constraints imposed by the fillers. They idealized the MMM as a lamella containing composite layers, in which each composite layer comprised two regions. The first region consisted of a polymer (R_m) and the second one of polymer and zeolite particles (mixed-region ($R_f - R_t$)). In this model, the polymer region was assumed to be in series with the parallel resistances of the second, mixed region.

Although the Te Hennepe model was originally developed for pervaporation of MMMs in liquid separation (ethanol–water), it has also been applied to gas separation studies, such as CO_2 and O_2 permeation in MMMs containing MFI zeolite, faujasite, and A-type zeolites with PDMS, Udel, PES, EPDM, NBR, PEI, CA, and TPX polymers. The model's predictions for gas permeability are consistent in order of magnitude with those from two-resistance models and the Maxwell model.[43,44]

2.3 Cussler model

Cussler *et al.*[45] developed a four-resistance model to describe gas transport in MMMs. This model considers a two-dimensional transport in the MMM, where the fillers are assumed to be permeable, flake structures uniformly and orderly dispersed in the polymer matrix. It assumed the resistance of the polymer region was in series with that of a second, mixed region, similar to Te Hennepe *et al.*[42] However, transport in the mixed region was assumed to occur in the permeation direction through the filler phase and perpendicular to the permeation direction through the polymer phase. This assumption led to eqn (5) in Table 1, in which $\lambda_f = w_f/l_f$ is the aspect ratio of the filler phase, with w_f and l_f being the flake width and thickness, respectively.

Notably, while the Cussler model does not incorporate explicit physical parameters to quantify spatial distribution, the researchers highlight that the spatial arrangement of flakes still plays a significant role in membrane performance. They note that although analyses based on randomly distributed flakes yield equivalent results, the highly oriented nature of the flakes in the idealized lamellar structure is critical for approaching the selectivity of layered composites, as poorly oriented flakes would lead to higher but less selective fluxes. By explicitly introducing the aspect ratio, the Cussler model establishes a direct quantitative relationship between filler geometry and membrane performance. Higher aspect ratio fillers, characterized by thinner and wider flake structures, create more efficient and selective transport pathways through the membrane. This geometric optimization enhances molecular sieving capability while maintaining gas permeability, demonstrating precisely how controlled manipulation of nanofiller dimensions directly governs both the selectivity and permeability of gas separation processes.

2.4 Ebneyamini model

Ebneyamini[46] proposed a semi-empirical four-resistance model to predict the permeability of ideal MMMs containing cubic fillers, as shown in eqn (6). An empirical correction factor τ was introduced to a one-dimensional four-resistance model. In this model, τ was estimated *via* simulation of the 3D particle-polymer system and adjusted to follow Langmuir-type equations. Thus, τ is assumed to accommodate tortuosity effects arising from large differences amongst the MMM constituent phase permeabilities. Moreover, the model suggests that this tortuosity effect becomes more pronounced with both increasing disparity between the permeabilities of the filler and polymer phases, and higher filler loading. τ, which is a function of the filler volume fraction φ_f and the permeability ratio of the filler to the polymer phase (P_f/P_m), is shown in Table 1. When $P_f/P_m > 1$, τ is calculated using eqn (7); when $P_f/P_m \leq 1$, τ is calculated using eqn (8). τ effectively correlates macroscopic membrane performance with underlying structural and material characteristics by capturing how the interplay between the filler loading and the intrinsic permeability disparity of the constituents influences mass transport.

2.5 KJN model (ideal interface)

The above resistance models are mainly used to predict the permeation performance of MMMs with cubic or platelet fillers. With the preparation of many tubular fillers, nanotube-MMMs have attracted more and more attention for their excellent performance.[6,16] However, modeling MMMs with a tubular filler has received less attention, with only a few studies developing RMA models for nanotube-MMMs.

The first of these RMA models was proposed by Kang *et al.*,[47] who accommodated the orientation of tubular fillers in the calculation of the overall transport resistance. The final model was named by the authors as the Kang–Jones–Nair (KJN) model. The model introduces the orientation angle θ of the filler ($\theta \in [0, \pi/2]$), measured with respect to the permeation direction, and the parameter λ_f ($\lambda_f = d_f/l_f$), which is the aspect ratio of the tubular filler, with d_f and l_f being the diameter and length of the cylindrical particle, respectively. For uniformly oriented fillers, the KJN model is expressed by eqn (9) in Table 1, while for randomly oriented fillers, it is given by eqn (10). Here, $P_{eff}^{oriented}(\theta)$ in eqn (10) is calculated from eqn (9).

The KJN model's incorporation of both orientation angle (θ) and aspect ratio parameter (λ_f) represents a seminal advancement in structure–performance modelling for MMMs. These parameters work synergistically to determine membrane performance by governing molecular orientation effects and transport pathway geometry. The model quantitatively predicts how the alignment of anisotropic fillers (θ) and their geometric proportions (λ_f) collectively influence permeability and selectivity. When high-aspect-ratio fillers (low λ_f) align parallel to the gas flux direction ($\theta = 0°$), they provide elongated selective channels that maximize performance, whereas random orientation significantly reduces efficiency through increased diffusion resistance. Higher λ_f values offer limited modulation capability due to the shorter transport paths. This dual-parameter framework establishes a fundamental design principle, demonstrating that coordinated control of both filler alignment and aspect ratio during membrane fabrication is

essential for achieving simultaneous optimization of permeability and selectivity.

The predictions of the KJN model are always lower than those based on effective medium methods such as the Maxwell model.[17] These differences are due to the fundamental dissimilarity of permeation paths in tubular fillers and isotropic fillers. Typical isotropic fillers such as zeolites or metal organic frameworks (MOFs), with three-dimensional interconnected channels, allow transport of gas molecules between the filler and the polymer matrix at any point of the interface of the two materials, whereas, for tubular fillers, the transport between the filler and the matrix can only take place at the tips of the filler. The "accessible surface area" of the fillers, which strongly correlates with their capability of enhancing the permeability for the matrix, can be quantitatively assessed.[47] Moreover, the self-consistency assessments conducted by Kang *et al.* further clarify the limitations of Maxwell-type models and highlight the advantages of the KJN model.[47] The Maxwell-type model fails when considering filler orientations that are far from the ideal ($\theta = 0$) orientation. Furthermore, it is more difficult to include the filler orientation in the Maxwell-type model. In summary, it can be concluded that the KJN model provides more accurate physical insights and broader applicability, and is a more appropriate model for permeation in membranes with tubular fillers.

2.6 COFp-PVAm model

In recent years, Wang Zhi and his research team[48] proposed a three-resistance model for COFp-PVAm (polyvinylamine) mixed matrix membranes with fixed carriers in the polymer matrix phase, as shown in eqn (11).

The model assumes that gas molecules are transported in a single direction from top to bottom, and the channels passing through the COFp filler can be integrated into uniformly and vertically distributed nanochannels with a length of L and a diameter of W. These nanochannels are located in the middle section of the membrane, and the distance from the nanochannels to the upper and lower surfaces of the membrane can be obtained by subtracting the length L of the nanochannels from the thickness T of the membrane. This model is applied to the CO_2/N_2 gas mixture, and all CO_2 transport behavior can be classified into two forms. In the first, the polymer matrix is the only route for CO_2 molecules. In the second, CO_2 molecules pass through the nanochannel with length L and through the polymer matrix with length $T - L$. Based on this, a parallel model combining polymer permeation resistance R_1 and polymer/filler permeation resistance R_2 is proposed. For the PVAm membranes, the performance can be regarded as reflecting a parallel connection of two of the first forms. When the transmembrane pressure is similar, the fluxes of the COFp-PVAm membranes (Q_m) and the Plame membranes (U_p) can be related *via* eqn (11). Here, Q_1 and Q_2 represent the fluxes of the first and second forms, respectively, and R_1 and R_2 represent the gas transport resistances of the first and second forms, respectively. If it is assumed that (1) the N_2 molecules do not pass through the nanochannels at low pressure and (2) the pressure difference and membrane area are constant, then the proportions of Q_1 and Q_2 can be calculated from the membrane performance.

2.7 KJN model (non-ideal interface)

The model developed in Sections 2.1–2.6 describes perfect membranes with no defects; however, different types of defects are often formed during composite membrane fabrication. Specifically, the incompatibility between the filler and the matrix can create a void space surrounding the fillers. Additionally, the membrane may contain pinholes extending from the feed to the permeate side of the membrane. Such defects can significantly affect the membrane performance. Hence, it is critical to include them in permeation models and quantitatively assess their impact.

When interfacial voids and pinholes are present, two additional permeation pathways are introduced. Firstly, gas molecules at the filler/matrix interface can either diffuse through the tubular channel or diffuse through the surrounding void space without entering the filler (since the side walls of the tubular channel are isolated from adjacent pores, the molecules can permeate directly without entering the filler). Secondly, a pinhole can be modelled as an isolated channel with a relatively high permeability that allows molecules to bypass the membrane. A membrane with these two types of defects can be modelled as comprising three parallel transport pathways in total. These include: (i) a defect-free membrane with tubular fillers, (ii) a membrane composed of matrix and voids, and (iii) a pinhole. Consequently, a parallel three-resistance model has been proposed, which includes a polymer-filler permeation resistance R_f, without interfacial defects, a polymer-interface void permeation resistance R_{ive}, and a pinhole permeation resistance R_P. Applying the resistances-in-parallel concept, the total permeability is calculated by combining the contributions of each pathway, weighted by its volume fraction,[49,50] as specified in eqn (12) in Table 1. Here, $P_{eff,f}$ and $P_{eff,v}$ are the effective permeabilities of the regions of the membrane composed of filler/matrix and void/matrix, respectively; P_p is the permeability of the pinhole, and φ_f, φ_v, φ_p and φ_m are the volume fractions of the imaginary pieces composed of filler/matrix, void/matrix, pinhole, and the polymer matrix, respectively. The volume fraction is constrained by conservation of volume: $\varphi_f + \varphi_v + \varphi_p + \varphi_m = 1$. The effective permeability $P_{eff,f}$ can be calculated using the ideal MMM eqn (10). The effective permeability ($P_{eff,v}$) of the piece containing the matrix and void spaces can be predicted by the Hamilton–Crosser model,[51,52] as shown in eqn (13), assuming that the void space is cylindrical in shape and the diffusion in the void space is isotropic. In eqn (13), P_v is the permeability in the void space. If the diffusion of the gas molecules in the pores follows the Knudsen diffusion mechanism and the dissolution follows the ideal gas law, then the permeability coefficient P_v is calculated using eqn (14). It is reasonable to assume that the pinholes follow the same permeation mechanism as the void spaces. Therefore, the permeability coefficient P_p can also be calculated using eqn (14).

In non-ideal interfaces, defect morphology, size, and content strongly affect membrane performance. Voids, which are nanoscale gaps around fillers, boost permeability *via* their high intrinsic permeability. They may preserve or even improve selectivity in highly selective matrices but reduce it in low-selectivity ones. Pinholes, through-membrane pores, drastically increase permeability but severely degrade selectivity by enabling unselective bypass. Larger sizes and higher content amplify these effects, with pinholes causing more drastic performance damage than voids at the same content.

2.8 mKJN model

In recent years, Saqid *et al.*[53] introduced pseudo-dispersed phase fillers that influence the interfacial layer and consequently overall gas permeabilities, which was ignored in existing models. The proposed model is referred to as the mKJN model, as shown in eqn (15). In eqn (15), φ_{NT} is the volume fraction of the filler, and $P_{eff,d}$ is the ideal mixed matrix membrane permeability, with all other parameters retaining their original definitions from the KJN model. The permeability $P_{eff,d}$ is calculated using eqn (16).[28] Here, $P_{eff,m}$ is the permeability of the polymer matrix, and φ_d is the volume fraction of the polymer/filler. $P_{eff,v}$ can be predicted using the HC model,[51] with its core assumptions being that the permeability of interfacial voids is identical to that of the pseudo-dispersed phase, and both exhibit isotropic characteristics in morphology (*e.g.*, cylindrical or tubular shapes). In these interfacial voids and pinholes with consistent properties, the transport of gas molecules is primarily governed by Knudsen diffusion. Therefore, the estimation of $P_{eff,v}$ can be performed using the HC model, as shown in eqn (17).[51,54] In eqn (17), P_{ps}, P_{NT}, and P_{int} denote the permeabilities of the pseudo-dispersed phase, fillers (*e.g.*, MWCNTs), and the interfacial layer, respectively. The permeability P_{int} is calculated using eqn (19),[55,56] where the thickness of the interface l_{int} is obtained by experimental fitting. In addition, φ_s denotes the volume fractions of the pseudo-dispersed phase and can be estimated by eqn (18) in Table 1.

The mKJN model establishes a quantitative structure–performance relationship by incorporating interfacial layer parameters. The permeability of this interphase (P_{int}) typically differs from that of the bulk polymer, as it is influenced by local nanoscale morphological alterations such as polymer chain rigidification at the filler surface, and directly governs overall membrane performance. By correlating macroscopic permeation data with interfacial parameters (P_{int}, l_{int}) through the mKJN model and analyzing concomitant changes in permeability and selectivity, researchers can quantitatively characterize key interfacial properties, including interaction strength, defect state, and local polymer morphology. This approach enables the reverse inference of interfacial quality based on macroscopic performance metrics.

2.9 Hashemifard model

In Hashemifard's work,[57] the permeability of an MMM is theoretically modeled with the aid of a combination of simple series-parallel gas flow arrangements, and a body-centered cubic (BCC) lattice is used to model the particle distribution throughout an MMM. The model is based on the two flow patterns of the permeant gas through the MMM element: (1) penetrant gas flow path through the MMM element for voids in the MMM and (2) penetrant gas flow path through the MMM element for rigidified MMM. Hashemifard *et al.*[57] divided the gas transport pathways in the MMM into three distinct regions: (1) zone I, consisting of continuous, interphase and dispersed phase, (2) zone II, consisting of continuous and interphase, and (3) zone III, consisting of continuous phase only. While the penetrant gas flows through the MMM element with voids, the gas permeates progressively through zone III, consisting of continuous phase only, then through zone II, consisting of continuous and interphase as a parallel channel, and finally through zone I, consisting of continuous, interphase and dispersed phase as a parallel channel. After zone I, the flow through zones II and III is repeated before the gas leaves the MMM element. While the penetrant gas flows through the MMM element for rigidified MMM, the gas permeates through zone III, consisting of continuous phase only, and through zone II, consisting of continuous and interphase as a series channel, as well through zone III, consisting of continuous, interphase and dispersed phase as a series channel. The flows through each of the zones are parallel to each other. The flows through the different zones are finally combined before leaving the MMM element.

Accordingly, the series or parallel three-resistance model (R_I, R_{II}, and R_{III}) for the permeability of MMMs was proposed, as shown in eqn (20). If the MMM forms interfacial voids, the series model is adopted with parameter $u = 1$; if a rigid interfacial layer is formed, the parallel model is applied with parameter $u = -1$. In the model, the ratio of the polymer/filler interface to the polymer permeability is defined as $\lambda_i = P_i/P_m$, while the ratio of the filler to the polymer permeability is $\lambda_d = P_f/P_m$. The interfacial thickness is denoted as t. φ_I, φ_{II}, and φ_{III} represent the volume fractions of zones I, II, and III in the entire MMM, respectively. φ_{di}, φ_{iI}, and φ_{mI} indicate volume fractions of the dispersed phase, interphase and continuous phase in zone I, respectively. φ_{iII} and φ_{mII} correspond to the volume fraction of the interphase and continuous phase in zone II, respectively. The model assumes the filler particles to be cylinders with equal aspect ratios ($d_L = d_r$), where d_p represents the diameter of a sphere with equivalent volume to the cylindrical filler. Therefore, the relationships between these three lengths are given by eqn (21):

$$d_L = \sqrt[3]{\frac{2}{3}} d_P \tag{21}$$

The model incorporates filler loading (φ), relative interphase thickness (θ), and the permeability ratios of filler (λ_d) and interphase (λ_i) to the polymer matrix. These parameters define membrane morphologies, including ideal, rigidified, leaky or void-rich structures, and govern the resulting permeability and selectivity. It demonstrates that higher filler loading enhances permeability when the filler itself has higher permeability than the polymer or when a leaky interphase is present. Conversely,

a rigidified interphase reduces permeability while potentially improving selectivity.

It has been proven that the experimental data are in good agreement with this pattern of gas flow through the MMM element. This reveals that the proposed model is capable of serving as a useful tool to understand gas flow behavior better and thus distinguish the differences between morphologies and their influences on gas permeabilities in MMMs.

3. Applications of the resistance model

3.1 Design optimization of membrane structures

By applying the ideal resistance model, the influence of factors such as the permeability ratio of fillers to polymers, filler orientation, aspect ratio, and size, on the effective permeability of MMMs can be analyzed, thereby providing guidance for regulating membrane structures to improve gas separation performance.[47,58–65]

MMMs with multiple transport mechanisms can utilize the ideal resistance model to estimate the relative contribution of each mass transfer mechanism for gas molecules within the membrane, thereby guiding structural optimization.[48,66] For example, the previously mentioned COFp-PVAm MMM combines dual mechanisms: (1) amine-facilitated transport and (2) surface diffusion through confined pore channels. By applying a dual-path resistance model (Path 1: diffusion through the pure polymer matrix; Path 2: series diffusion through amine-functionalized channels and partial polymer matrix), the contributions of these two mechanisms can be quantified. The experimental results obtained by Wang *et al.*[48] show that a higher contribution from Path 2 leads to greater CO_2 permeance. Specifically, in COF_a-PVAm(M), Path 2 accounts for 61%, yielding a CO_2 permeance of 1168 GPU, while in COF_a-PVAm(H), Path 2 increases to 65%, further boosting CO_2 permeance to 1952 GPU. By precisely tuning the parameters such as filler loading and polymer molecular weight, the Path 2 contribution can be enhanced, enabling the design of high-performance CO_2 separation membranes.

Non-ideal resistance models can be employed to analyze the influence of polymer/filler interfaces and filler permselectivity on the overall performance of MMMs, thereby providing a theoretical basis for the optimized design of membrane structures.[47,53,57,67] Yu *et al.*[67] applied the permeation model for non-ideal MMMs proposed by Hashemifard *et al.*[57] to the UiO-AcOH-1.4/PIM-1 system, focusing on investigating the effects of filler loading, interface performance parameters (the ratio of the permeability at the polymer/filler interface to that of the polymer matrix, $\lambda_i = P_i/P_m$), and filler performance parameters (the ratio of the permeability of the filler to that of the polymer matrix, $\lambda_d = P_f/P_m$) on the permeation performance of the MMM. The results showed that when the filler loading was 15 wt%, the CO_2 permeability of the MMM significantly approached the leakage curve ($\lambda_i = 5$), indicating minimal interfacial resistance. Moreover, the λ_d value was much larger than λ_i, suggesting that gas molecules preferentially diffuse through the highly permeable UiO-AcOH-1.4 filler rather than the interfacial gaps, confirming the critical role of filler permeability in enhancing overall membrane performance.

Additionally, the model analysis demonstrated that uniform filler dispersion and interfacial compatibility are key factors for achieving high λ_d values and low interfacial resistance. The uniform filler dispersion ensures that the highly permeable UiO-AcOH-1.4 fillers are evenly distributed throughout the PIM-1 matrix, maximizing the number of effective gas transport channels. This avoids filler aggregation (as observed when the filler content exceeds 15 wt%), which would otherwise create barriers to gas diffusion and reduce the overall permeability of the dispersed phase, thus lowering the λ_d value.

Superior interfacial compatibility is key to minimizing interfacial resistance, which is reflected in the λ_i value approaching the leaky curve condition ($\lambda_i = 5$). It effectively suppresses the formation of non-selective interfacial defects caused by phase incompatibility. This intimate interfacial contact facilitates seamless gas transport between the filler and polymer matrix, significantly reducing the energy barrier for interfacial mass transfer. Consequently, gas molecules preferentially diffuse through the high-permeability filler phase (the high-λ_d path) rather than being hindered by interfacial resistance.

Surface modification of the filler or interfacial engineering techniques can further enhance this compatibility by adjusting the chemical interactions between the filler and the polymer chains, ensuring that the filler remains well-dispersed and the interface remains intact, which are crucial for optimizing the λ_d and λ_i parameters.

Through KJN model analysis, it was further revealed that the interfacial effect between the polymer and the filler exerts dual regulatory effects on membrane performance. For polymer matrices with high selectivity but low permeability (such as traditional glassy polymers), the formation of interfacial gaps can simultaneously enhance both permeability and selectivity. However, for polymer matrices with high permeability but low selectivity, interfacial voids may improve permeability at the expense of selectivity due to increased non-selective diffusion pathways.[47,68] This conclusion provides a theoretical basis for the appropriate selection of fillers and polymers in MMMs, and offers guidance for regulating polymer/filler interface interactions. For instance, MMMs combining highly selective fillers with molecular sieve effects (*e.g.*, defect-engineered MOFs) with high-free-volume polymers (*e.g.*, PIM-1) can suppress non-selective diffusion through optimized interfacial interactions, achieving a synergistic improvement in both permeability and selectivity.[67]

In addition to evaluating the permeation performance of MMMs using the series resistance model, this modeling approach can also be applied to investigate gas transport resistance distribution in multilayer composite membranes,[69,70] thereby providing guidance for membrane structural design and optimization. A representative application was demonstrated by Sánchez-Laínez *et al.*[70] in their study of ZIF-8-polybenzimidazole (PBI)/polydimethylsiloxane (PDMS)/P84® MMMs. The authors employed a three-resistance series model

to decompose the overall transport resistance into: (1) resistance from the PDMS-coated surface layer, (2) resistance through the ZIF-8-PBI selective skin layer, and (3) substructure resistance from the porous P84® support layer. Using this model, the resistance values of each component were calculated. For the PBI/PDMS/P84® composite membrane, the skin layer resistance derived from self-supported asymmetric PBI membranes was calculated to be 1/2.1 GPU^{-1}, and the substructure resistance was calculated to be 0.24 GPU^{-1}. Compared with the PBI/PDMS/P84® composite membrane, the introduction of ZIF-8 reduced both the skin layer resistance (1/3.0 GPU^{-1} obtained from the literature) and the support layer resistance (0.12 GPU^{-1} calculated from the three-resistance series model). The lower resistance values compared to bare PBI membranes imply that the filler is distributed not only in the skin layer but also within the substructure. This is mainly attributed to two aspects: on the one hand, the molecular sieve pores of ZIF-8 provide a rapid diffusion path for gas molecules, significantly improving the permeability of the skin layer (for example, in the experiment, the H_2 permeance increased from 6.5 GPU to 22.4 GPU); on the other hand, the partial dispersion of ZIF-8 nanoparticles in the support layer increases the connectivity of the porous structure, thereby reducing the tortuosity of gas transport and improving the permeability of the porous support layer. This model successfully quantifies the effect of filler addition on the transfer resistance of MMMs with a multilayer structure, providing a quantitative design basis for the structural optimization of MMMs.

3.2 Prediction of effective permeability

Several resistance models demonstrating excellent agreement with experimental data are presented in Table 2. The agreement between experimental data and theoretical models for gas permeability in MMMs was evaluated using the average absolute relative error (AARE%), as shown in eqn (22).

$$\mathrm{AARE\%} = \frac{100}{N}\sum_{i=1}^{N}\left|\frac{P_i^{\mathrm{cal}} - P_i^{\mathrm{exp}}}{P_i^{\mathrm{exp}}}\right| \quad (22)$$

where N is the number of the data points, and P_i^{exp} and P_i^{cal} are the experimental and estimated permeabilities, respectively. Lower AARE% values indicate better model accuracy, meaning the model predictions more closely match the experimental results.

Ideal models can accurately predict the permeation performance of MMMs with good polymer-filler compatibility. The KJN model demonstrates excellent agreement with experimental permeation data for MMMs incorporating tubular fillers. Using the KJN model to predict the CO_2 permeability of NH_2-MWCNT/polyvinyl alcohol (PVA) membranes under a feed gas mixture of 20 vol% CO_2, 59.8 vol% CH_4, 20.2 vol% H_2, the average absolute relative error (AARE) was calculated to be 0.26% for MMMs with filler loadings of 0 vol% and 3 vol%.[60,71] In addition, the KJN model also exhibits high prediction accuracy for the pure CO_2 permeability of PMMA-MWCNT/polyamide (PA) and COOH-SWCNT/brominated poly (2,6-diphenyl-1,4-phenylene oxide) (BPPOdp) membranes,[60] with specific AARE% values shown in Table 2.

The Cussler model demonstrates excellent predictive performance for permeability in MMMs containing 2D flake-shaped fillers.[72–74] Compared to the Maxwell model and Bruggeman model of the effective medium method, the Cussler model has better prediction accuracy for anisotropic flake fillers because it takes into account the shape and size factors of the fillers. Buddin *et al.*[73] demonstrated the accuracy of the Cussler model in predicting CO_2 permeability of ZIF-L/PDMS/PES MMMs containing 2D flake-like fillers, achieving an average absolute relative error of just 0.7%. For zeolite MFI-PTMSP (polytrimethylsilyl-1-propyne) MMMs used in *n*-butane/isobutane separation, the Cussler model provided highly accurate predictions at a low filler loading of 3 vol%. However, at higher loadings, significant discrepancies between the calculated and experimental values were observed. The authors attributed this to severe particle agglomeration of the zeolite MFI fillers, which deviates from the Cussler model's assumption of uniformly aligned fillers, thus leading to large errors. The authors further emphasized that well-aligned, high-aspect-ratio MFI nanosheets in a compatible, highly permeable polymer matrix can achieve high gas separation performance even at low filler loadings.[74] For non-ideal MMMs, the influence of the permeability at the polymer/filler interface on the overall permeability of the membrane cannot be ignored.[47,53,57] Saqid modified the KJN model by incorporating non-ideal interfacial effects to describe the MWCNTs-PSF (polysulfone) membrane system. When tested with pure gases (CO_2, N_2, and CH_4), the modified model demonstrated average absolute relative errors ranging from 1.2588% to 10.8046%, whereas the original KJN model showed a substantially higher error of approximately 52.43% for the same MWCNTs-PSF system,[53] as detailed in Table 2. It can be seen that for the prediction of permeability in non-ideal MMMs, the accurate prediction of permeability at the polymer/filler interface is crucial. The Hashemifard model demonstrates excellent agreement with experimental data when predicting permeability in MMMs composed of zeolites or carbon molecular sieves. For O_2/N_2 separation, the Hashemifard model accurately predicts the permselectivity of MMMs containing zeolite NaA with polymers such as polyether sulfone (PES), Matrimid 5218, polyimide (PI), and Ultem 1000. Meanwhile, for both CO_2/CH_4 separation and O_2/N_2 separation, the model also achieves high prediction accuracy in evaluating the permeability and selectivity of MMMs composed of carbon molecular sieves (CMS) and Matrimid 5218.[57]

Recently, Asif *et al.*[75] combined the simple parallel resistance model (a macroscopic model) with molecular simulation (a mesoscopic and microscopic method) to predict the permeation performance of MMMs. The solubility and diffusion coefficients calculated *via* Monte Carlo (MC) and molecular dynamics (MD) provide an atomic-scale basis for parameters such as Henry's constant and affinity constant in the resistance model. This highlights the importance of molecular simulation work in selecting and developing appropriate empirical models that can be used to describe gas transport behavior according to the filler-polymer system of interest in a relatively convenient and

Table 2 Mean absolute relative error: experimental *vs.* theoretical values for the selected resistance models

Membrane materials polymer + filler	Gas composition	Model	Average absolute relative error % (AARE%)	References
PVA-Raw-MWCNT (0 vol%, 1 vol%, 2 vol%, 4 vol%)	CO_2 (20 vol% CO_2, 40 vol% H_2, 40 vol% N_2)	KJN	0.5200	56 and 60
PVA-NH_2-MWCNT (0 vol%, 3 vol%)	CO_2 (20 vol% CO_2, 59.8 vol% CH_4, 20.2 vol% H_2)	KJN	0.2600	60 and 71
PA-PMMA-MWCNT (0 vol%, 2 vol%)	Pure CO_2	KJN	1.8900	60
BPPOdp-COOH-SWCNT (0 vol%, 3vol%)	Pure CO_2	KJN	0.9700	60
PDMS/PES-ZIF-L (1.82 wt%)	Pure CO_2	Cussler	0.7000	73
PSF-Raw-MWCNTs (5wt%, 10wt%, 20wt%)	Pure CO_2	mKJN	10.8046	53
	Pure CH_4		4.3125	
	Pure N_2		3.5559	
PSF-OH-MWCNTs (5wt%, 10wt%, 20wt%)	Pure CO_2	mKJN	1.6751	53
	Pure CH_4		2.8839	
	Pure N_2		1.2588	
PSF-amine-MWCNTs (5wt%, 10wt%, 20wt%)	Pure CO_2	mKJN	7.5414	53
	Pure CH_4		7.6897	
	Pure N_2		7.3849	

cost-efficient way, as compared to experimental investigation. Furthermore, extending beyond conventional empirical models limited to pure gas analysis, this parallel resistance model explicitly accounts for the interdependent influences of filler concentration (15–30 wt% silica) and mixed-gas feed composition (CO_2/CH_4 ratios of 30/70, 50/50, and 70/30) on both permeability and solubility coefficients. Firstly, the incorporation of silica nanoparticles (increasing filler loading) disrupts polymer chain packing, increasing the fractional free volume (FFV) and creating additional pathways for gas transport. However, the feed composition determines how these new pathways are utilized. In CO_2/CH_4 mixtures, CO_2 molecules exhibit stronger competitive adsorption and higher diffusivity. Therefore, as the CO_2 concentration in the feed increases, it preferentially occupies the newly created transport pathways, leading to a more significant boost in overall permeability compared to what would be expected from simply adding the effects of filler loading and gas composition independently. Secondly, the pure gas solubility values are consistently higher than those under mixed-gas conditions due to competitive sorption. The addition of filler introduces new sorption sites, but the gas composition determines which species occupies them. CO_2, having a higher affinity, competitively inhibits CH_4 sorption, especially at higher CO_2 feed concentrations. This suppression of CH_4 solubility is a direct result of the interaction between the filler (providing sites) and the composition (triggering competition). Finally, the correlation between filler loading and gas composition is nonlinear. Excessive filler (*e.g.*, 30 wt% silica) causes agglomeration, which reduces the effective interfacial area, forms non-uniform pore structures, and disrupts the continuity of free volume and adsorption sites. Consequently, the physical barrier effect of agglomerates dominates the transport pathways, and the influence of gas composition is significantly weakened. Even if the CO_2 concentration increases, its preferential utilization of transport pathways is hindered by the agglomerated structure, the competitive adsorption between CO_2 and CH_4 weakens, and the dependence of membrane performance on gas composition decreases, breaking the synergistic coupling observed at lower loadings ($\leq$25 wt% silica). The parallel resistance model, as proposed by Asif *et al.*, incorporates both filler weight fraction and gas mole fraction, thereby quantitatively characterizing the filler–composition interdependence, which is a critical factor governing the model's accuracy in predicting mixed-gas feed performance.

In summary, resistance models demonstrate significant advantages in predicting the permeability of MMMs with tubular/flake-like fillers and guiding membrane structure optimization, with their applicability inherently linked to filler shape and distribution characteristics. For tubular fillers, their high aspect ratio leads to orientation-dependent distribution (*e.g.*, parallel, tilted, or random relative to the permeation direction), which directly affects transport pathways. The KJN model, by incorporating the orientation angle (θ) and the aspect ratio (λ_f), effectively captures these shape-distribution effects to optimize membrane structure design, while the mKJN model, by incorporating the permeability of the interface (P_{int}) and the thickness of the interface (l_{int}), further refines predictions by accounting for non-ideal interfacial structures (*e.g.*, interfacial voids) to provide more accurate permeability predictions. For MMMs with non-ideal interfaces and molecular sieving fillers (*e.g.*, zeolites), the Hashemifard model relies on the assumption of uniformly distributed fillers (*e.g.*, *via* a BCC lattice representation) and focuses on analyzing the influence of interfacial defects on interfacial resistance. By precisely characterizing interfacial properties (*e.g.*, relative interphase thickness (θ), the permeability ratios of the interphase to the polymer matrix (λ_i)), this method enables accurate prediction of permeability and optimization of membrane structure. For flake-like fillers, their planar geometry demands ordered alignment to leverage in-plane permeability. For instance, the Cussler model, which integrates aspect ratio ($\lambda_f = w_f/l_f$) and assumes uniform

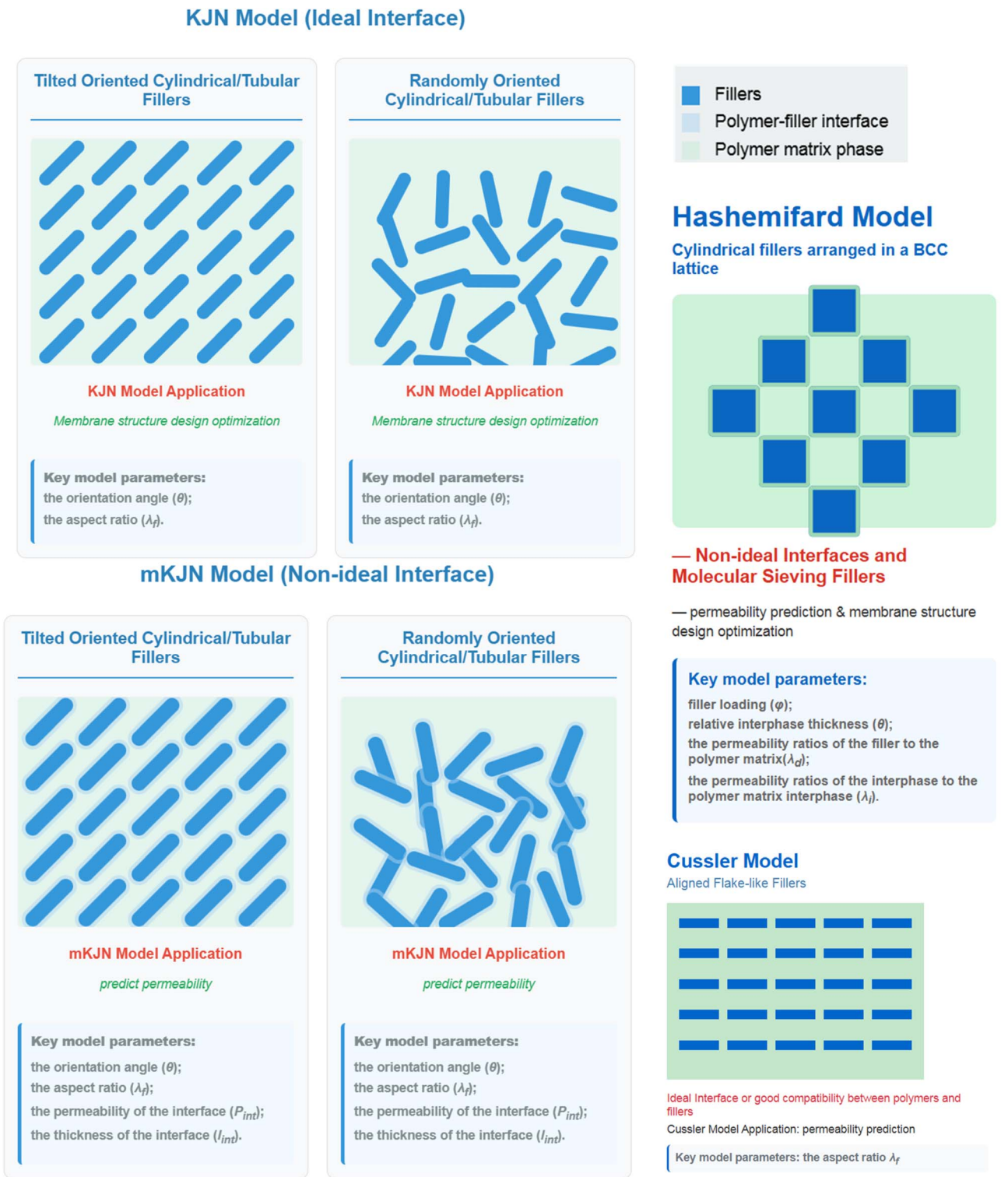

Fig. 1 Comparative analysis of resistance models for MMMs.

dispersion, thus provides reliable permeability predictions for MMMs with ideal interfaces or good polymer-filler compatibility, where ordered distribution maximizes shape-dependent transport advantages.

A comparative analysis of these resistance models for MMMs in terms of their structures and applications is presented in Fig. 1. The framework is derived from the comparative analysis presented in this work, illustrating the applicability of each model for predicting permeability and/or optimizing

membrane design under specific conditions: (i) the KJN model is suited for MMMs with oriented or randomly distributed tubular/cylindrical fillers and ideal interfaces; (ii) the mKJN model extends the KJN model to account for non-ideal interfaces in tubular filler systems; (iii) the Hashemifard model is applicable to systems with non-ideal interfaces and molecular sieving fillers, the distribution of which is described *via* a body-centered cubic (BCC) lattice arrangement; (iv) the Cussler model is recommended for flake-like fillers with ordered alignment, ideal interfaces, or good polymer-filler compatibility.

4. Conclusions

Membrane separation technology, as a critical approach for energy-efficient gas separation, has long been constrained by the lack of systematic design principles for MMMs incorporating anisotropic nanofillers (*e.g.*, nanotubes, nanosheets) and the limitations of conventional models in dealing with complex transport behaviors. A fundamental challenge lies in establishing quantitative links between multifaceted membrane morphology and separation performance. This work addressed these critical bottlenecks by systematically investigating the RMA-based models, aiming to strengthen the guiding role of models in accelerating the development of high-performance MMMs.

By reviewing classic RMA-based models (*e.g.*, Series and Parallel Resistance Models, and the Te Hennepe, Cussler, KJN, mKJN, and Hashemifard models), we clarified their underlying principles, application boundaries, and practical value. The findings reveal that, unlike effective medium theory (EMT), which assumes randomly distributed spherical fillers, RMA exhibits superior applicability for MMMs with oriented cubic, flake-like, or tubular fillers. Specifically, for MMM containing carbon nanotubes or zeolite nanosheets, RMA is better than the Maxwell model and other EMT-based models in predicting permeability; this solves the problem faced by traditional models that cannot capture anisotropic transport behavior. For MMMs containing 3D fillers such as 3D zeolites or molecular sieves, models such as the Hashemifard model, which divides transport regions into a continuous phase, interfacial phase, and dispersed phase, have shown good agreement with experimental data (with low AARE%).

Furthermore, this study established a holistic framework for RMA model selection by quantifying prediction accuracy *via* the average absolute relative error (AARE%). By distinguishing the differential advantages of RMA variants, such as KJN for tubular fillers, Cussler for 2D flakes, and mKJN for tubular fillers with non-ideal interfaces, we resolved the model selection dilemma, enabling precise matching between models and membrane systems. This framework addresses the absence of systematic design principles accounting for filler orientation and interface effects.

Notably, we transformed RMA from a mere predictive tool into a design guide by demonstrating its utility in optimizing filler loading, orientation, and interfacial engineering. Case studies (*e.g.*, COFp-PVAm membranes analyzed *via* dual-path resistance models, and structural optimization of tubular filler-based MMMs using the KJN model) validated that RMA can quantify the contributions of mass transfer pathways, filler effects, and interface mechanisms, thereby providing actionable insights for performance-enhanced membrane design. This shift from prediction to design addresses the limitations of conventional models in guiding the rational design of structurally heterogeneous MMMs.

This review has systematically shown that the Resistance Model Approach (RMA) offers more than just predictive equations for permeability. It establishes a vital quantitative link between the multifaceted morphology of MMMs and their gas separation performance. From filler geometry (aspect ratio, orientation) to interfacial morphology (voids, rigidified layers), each RMA model describes how a specific structural feature translates into a distinct mass transfer resistance, thereby providing an integrated and mechanistic framework for designing high-performance membranes. In summary, this work strengthens the theoretical foundation for MMM design by advancing RMA's application in both permeability prediction and structural optimization, providing valuable guidance for the development of high-performance gas separation membranes and ultimately promoting the advancement of membrane separation technology.

While this study confirms the superiority of RMA in predicting permeability for anisotropic filler-based membranes, its accuracy requires further refinement to better guide membrane fabrication.

Firstly, the non-ideal interactions at polymer/filler interfaces are often oversimplified in current RMA variants. Empirical formulas and experimental data fitting for interface thickness are generally adopted to calculate the permeation performance at the interface, which affects the model accuracy and applicability. Therefore, future resistance model approaches should be integrated with other simulation methods to thoroughly investigate the relationship between the interfacial microstructure and the permeation performance of MMMs, such as finite element analysis (a rigorous simulation-based modeling method), molecular dynamics simulation and density functional theory (mesoscopic and microscopic scale analysis methods), as well as advanced characterization techniques (*e.g.*, infrared microimaging (IRM)). This integrated approach is crucial for clarifying the influence of the mechanism of polymer-filler compatibility, interface modifiers, and filler size and shape on polymer-filler interactions, which are of great significance for the design and development of high-performance MMMs.

Secondly, the transport coefficients of porous fillers are typically derived from empirical formulas, neglecting their intrinsic structural heterogeneity. Machine learning algorithms (*e.g.*, graph neural networks) can decode the relationship between 3D pore architectures (*e.g.*, tortuosity, connectivity) and gas transport coefficients, thereby significantly enhancing model accuracy.

Finally, due to the limitations of the fundamental assumptions in the resistance model, future models should also account for the effects of isothermal nonlinearity and the finite-

size effects of membranes on permeation performance. These issues can be addressed using isothermal nonlinear models, such as the Langmuir model, as well as rigorous simulation-based modeling approaches.

Conflicts of interest

There are no conflicts to declare.

Data availability

The data supporting the findings of this review are derived from previously published studies, which are cited in the references section. All relevant data, including permeability coefficients, model parameters, and experimental results analyzed in this work, are available in the original publications listed in the references (*e.g.*, ref. 1–75). Specific datasets can be accessed through corresponding journals or repositories referenced therein. No new primary data were generated in this review.

Acknowledgements

The work was supported by the Joint Science and Technology Project of Bijie (Bikelianhe [2023]14), the Joint Science and Technology Project of Bijie (Bikelianhe [2023]35), the Joint Fund of Bijie City and Guizhou University of Engineering Science (Bikelianhe [2025]43), the Key Laboratory for Research and Development of New Lithium-ion Battery Materials (Qianjiaoji [2023]028), the National College Students Innovation and Entrepreneurship Training Program (2024106680224), and the National College Students Innovation and Entrepreneurship Training Program (2024106680229).

Notes and references

1 G. Li, W. Kujawski, R. Válek and S. Koter, *Int. J. Greenhouse Gas Control*, 2021, **104**, 103195.
2 Y. Fan, W. Yu, A. Wu, W. Shu and Y. Zhang, *RSC Adv.*, 2024, **14**, 20714.
3 M. Farnam, H. bin Mukhtar and A. B. Shariff, *ChemBioEng Rev.*, 2021, **8**, 90–109.
4 X. Y. Wen, Y. H. Chen, W. G. Wang, Y. H. Niu, S. S. He, B. S. Ge and H. X. Sun, *Sep. Purif. Technol.*, 2025, **376**, 134080.
5 M. I. F. Zainuddin and A. L. Ahmad, *J. CO_2 Util.*, 2022, **62**, 102094.
6 Z. Niu, N. He, Y. Yao, A. Ma, E. Zhang, L. Cheng, Y. Li and X. Lu, *Chem. Eng. J.*, 2024, **494**, 152912.
7 C. H. Wu, K. X. Zhang, H. L. Wang, Y. Q. Fan, S. W. Zhang, S. F. He, F. Wang, Y. Tao, X. W. Zhao, Y. B. Zhang, Y. H. Ma, Y. J. Lee and T. Li, *J. Am. Chem. Soc.*, 2020, **142**, 18503–18512.
8 H. Wang, S. He, X. Qin, C. Li and T. Li, *J. Am. Chem. Soc.*, 2018, **140**, 17203–17210.
9 T. Xu, P. P. Zhang, F. C. Cui, J. T. Li, L. Kan, B. B. Tang, X. Q. Zou, Y. L. Liu and G. S. Zhu, *Adv. Mater.*, 2023, **35**, 2204553.
10 B. H. Monjezi, K. Kutonova, M. Tsotsalas, S. Henke and A. Knebel, *Angew. Chem., Int. Ed.*, 2021, **60**, 15153–15164.
11 K. Eum, S. Yang, B. Min, C. Ma, J. H. Drese, Y. Tamhankar and S. Nair, *ACS Appl. Mater. Interfaces*, 2020, **12**, 27368–27377.
12 X. Li, J. Hou, R. Guo, Z. Wang and J. Zhang, *ACS Appl. Mater. Interfaces*, 2019, **11**, 24618–24626.
13 M. Kim, W. Choi, C. H. Lee and D. W. Kim, *ACS Mater. Au*, 2024, **4**, 148–161.
14 L. Hu, K. Clark, T. Alebrahim and H. Lin, *J. Membr. Sci.*, 2022, **644**, 120140.
15 C. Y. Zhu, Y. Peng, K. Li, L. L. Liu and W. S. Yang, *J. Membr. Sci.*, 2024, **709**, 123140.
16 S. Rafiq, M. Saeed, A. Jamil, M. I. Rashid, M. Irfan, T. Iqbal, A. Inayat, F. Jamil, J. Iqbal, M. S. Khurram and M. S. Mehadi, *ChemBioEng Rev.*, 2023, **10**, 480–490.
17 G. M. Monsalve-Bravo and S. K. Bhatia, *Processes*, 2018, **6**, 172.
18 Q. Qian, P. A. Asinger, M. J. Lee, G. Han, K. M. Rodriguez, S. Lin, F. M. Benedetti, A. X. Wu, W. S. Chi and Z. P. Smith, *Chem. Rev.*, 2020, **120**, 8162–8266.
19 A. Riaz, L. Liu, Z. Xu, Q. Liu, M. Younas, J. Li, C. Luo and X. Ma, *Sep. Purif. Technol.*, 2024, **343**, 127175.
20 J. Liu, C. R. P. Fulong, L. Hu, L. Huang, G. Zhang, T. R. Cook and H. Lin, *J. Membr. Sci.*, 2020, **606**, 118122.
21 G. M. Monsalve-Bravo and S. K. Bhatia, *J. Membr. Sci.*, 2018, **550**, 110–125.
22 G. M. Monsalve-Bravo and S. K. Bhatia, *J. Membr. Sci.*, 2017, **531**, 148–159.
23 A. N. V. Azar, S. Velioglu and S. Keskin, *ACS Sustainable Chem. Eng.*, 2019, **7**, 9525–9536.
24 E. Chehrazi, *ACS Omega*, 2024, **9**, 33425–33436.
25 K. Asif, S. S. Lock, S. A. A. Taqvi, N. Jusoh, C. L. Yiin, B. L. F. Chin and A. C. M. Loy, *Polymers*, 2021, **13**, 2199.
26 S. He, B. Zhu, X. Jiang, G. Han, S. Li, C. H. Lau, Y. Wu, Y. Zhang and L. Shao, *Proc. Natl. Acad. Sci. U. S. A.*, 2022, **119**, e2114964119.
27 Y. Liu, F. Guo, J. Hu, H. Liu and Y. Hu, *AIChE J.*, 2017, **63**, 4586–4593.
28 H. Vinh-Thang and S. Kaliaguine, *Chem. Rev.*, 2013, **113**, 4980–5028.
29 S. Keskin and S. A. Alsoy Altinkaya, *Computation*, 2019, **7**, 36.
30 J. Winarta, A. Meshram, F. Zhu, R. Li, H. Jafar, K. Parmar, J. Liu and B. Mu, *J. Polym. Sci.*, 2020, **58**, 2518–2546.
31 S. Velioglu, H. E. Karahan and S. B. Tantekin-Ersolmaz, *Sep. Purif. Technol.*, 2024, **340**, 126743.
32 H. Daglar, I. Erucar and S. Keskin, *Mater. Adv.*, 2021, **2**, 5300–5317.
33 K. Kalauni, A. Vedrtnam, M. Wdowin and S. Chaturvedi, *Processes*, 2022, **10**, 2689.
34 F. Abdollahi, A. Khosravi, S. Karagöz and A. Keshavarz, *Appl. Energy*, 2025, **381**, 125203.
35 J. M. S. Henis and M. K. Tripodi, *J. Membr. Sci.*, 1981, **8**, 233.
36 I. Pinnau, J. G. Wijmans, I. Blume, T. Kuroda and K. V. Peinemann, *J. Membr. Sci.*, 1988, **37**, 81–88.
37 S. K. Karode, V. S. Patwardhan and S. S. Kulkarni, *J. Membr. Sci.*, 1996, **114**, 157–170.

38 J. L. Lopez, S. L. Matson, J. Marchese and J. A. Quinn, *J. Membr. Sci.*, 1986, **27**, 301–325.
39 A. Fouda, Y. Chen, J. Bai and T. Matsuura, *J. Membr. Sci.*, 1991, **64**, 263–271.
40 J. Winarta, A. Meshram, F. Zhu, R. Li, H. Jafar, K. Parmar, J. Liu and B. Mu, *J. Polym. Sci.*, 2020, **58**, 2518–2546.
41 C. M. Zimmerman, A. Singh and W. J. Koros, *J. Membr. Sci.*, 1997, **137**, 145–154.
42 H. J. C. Te Hennepe, C. A. Smolders, D. Bargeman and M. H. V. Mulder, *Sep. Sci. Technol.*, 1991, **26**, 585–596.
43 H. J. C. Te Hennepe, W. B. F. Boswerger, D. Bargeman, M. H. V. Mulder and C. A. Smolders, *J. Membr. Sci.*, 1994, **89**, 185–196.
44 A. Erdem-Şenatalar, M. Tatlier and Ş. B. Tantekin-Ersolmaz, *Chem. Eng. Commun.*, 2003, **190**, 677–692.
45 E. L. Cussler, *J. Membr. Sci.*, 1990, **52**, 275–288.
46 A. Ebneyamini, H. Azimi, F. H. Tezel and J. Thibault, *J. Membr. Sci.*, 2017, **543**, 351–360.
47 D. Y. Kang, C. W. Jones and S. Nair, *J. Membr. Sci.*, 2011, **381**, 50–63.
48 X. Cao, Z. Wang, Z. Qiao, S. Zhao and J. Wang, *ACS Appl. Mater. Interfaces*, 2019, **11**, 5306–5315.
49 D. Q. Vu, W. J. Koros and S. J. Miller, *J. Membr. Sci.*, 2003, **211**, 335–348.
50 T. T. Moore, R. Mahajan, D. Q. Vu and W. J. Koros, *AIChE J.*, 2004, **50**, 311–321.
51 R. L. Hamilton and O. K. Crosser, *Ind. Eng. Chem. Fundam.*, 1962, **1**, 187–191.
52 S. K. Das, S. U. S. Choi and H. E. Patel, *Heat Transfer Eng.*, 2006, **27**, 3–19.
53 S. Saqib, S. Rafiq, N. Muhammad, A. Laeeq Khan, A. Mukhtar, N. Binti Mellon, Z. Man, S. Ullah, A. G. Al-Sehemi and F. Jamil, *Chem. Eng. Sci.*, 2020, **218**, 115543.
54 S. A. Hashemifard, A. Ismail and T. Matsuura, *J. Membr. Sci.*, 2010, **347**, 53–61.
55 S. Wang, X. Li, H. Wu, Z. Tian, Q. Xin, G. He, D. Peng, S. Chen, Y. Yin, Z. Jiang and M. D. Guiver, *Energy Environ. Sci.*, 2016, **9**, 1863–1890.
56 H. Vinh-Thang and S. Kaliaguine, *J. Membr. Sci.*, 2014, **452**, 271–276.
57 S. A. Hashemifard, A. F. Ismail and T. Matsuura, *J. Membr. Sci.*, 2010, **350**, 259–268.
58 A. Jamil, O. P. Ching and A. M. Shariff, *Appl. Clay Sci.*, 2017, **143**, 115–124.
59 A. Zamani, F. H. Tezel and J. Thibault, *Membranes*, 2021, **11**, 58.
60 E. Chehrazi, A. Sharif, M. Omidkhah and M. Karimi, *ACS Appl. Mater. Interfaces*, 2017, **9**, 37321–37331.
61 M. Sarfraz, A. Arshad and M. Ba-Shammakh, *Arabian J. Sci. Eng.*, 2021, **47**, 6167–6179.
62 J. A. Sheffel and M. Tsapatsis, *J. Membr. Sci.*, 2009, **326**, 595–607.
63 J. Choi and M. Tsapatsis, *J. Am. Chem. Soc.*, 2010, **132**, 448–449.
64 A. Galve, D. Sieffert, E. Vispe, C. Téllez, J. Coronas and C. Staudt, *J. Membr. Sci.*, 2011, **370**, 131–140.
65 A. K. Zulhairun and A. F. Ismail, *J. Membr. Sci.*, 2014, **468**, 20–30.
66 H. Xu, S. G. Pate and C. P. O'Brien, *Chem. Eng. J.*, 2023, **460**, 141728.
67 J. Yu, Z. Wang, C. Yang, F. Wang, Y. Cheng, S. Wang, Y. Zhang and Z. Wang, *J. Environ. Chem. Eng.*, 2023, **11**, 110672.
68 R. Lin, B. V. Hernandez, L. Ge and Z. Zhu, *J. Mater. Chem. A*, 2018, **6**, 293–312.
69 O. Selyanchyn, R. Selyanchyn and S. Fujikawa, *ACS Appl. Mater. Interfaces*, 2020, **12**, 33196–33209.
70 J. Sánchez-Laínez, B. Zornoza, C. Téllez and J. Coronas, *J. Membr. Sci.*, 2018, **563**, 427–434.
71 L. Ansaloni, Y. Zhao, B. T. Jung, K. Ramasubramanian, M. G. Baschetti and W. W. F. Ho, *J. Membr. Sci.*, 2015, **490**, 18–28.
72 A. Jamil, O. P. Ching, M. Naqvi, H. A. A. Khan and S. R. Naqvi, *Processes*, 2020, **8**, 118.
73 M. M. H. S. Buddin, A. L. Ahmad and M. I. F. Zainuddin, *Membranes*, 2023, **13**, 134.
74 W. Choi, J. Park, E. Choi, M. Kim, H. Ji, O. Kwon, D. Kim and D. W. Kim, *J. Membr. Sci.*, 2023, **677**, 121659.
75 K. Asif, S. S. M. Lock, S. A. A. Taqvi, N. Jusoh, C. L. Yiin, B. L. F. Chin and A. C. M. Loy, *Polymers*, 2021, **13**, 2199.